JOURNAL OF GEOPHYSICAL RESEARCH, VOL. 106, NO. D24, PAGES 33,799–33,811, DECEMBER 27, 2001

High-resolution radar mapping of internal layers at the North Greenland Ice Core Project

P. Kanagaratnam, S. P. Gogineni, Niels Gundestrup,[1] and Lars Larsen[1]
Radar Systems and Remote Sensing Laboratory, University of Kansas, Lawrence, Kansas

Abstract. Existing accumulation maps with reported errors of about 20% are determined from sparsely distributed ice cores and pits. A more accurate accumulation rate might be obtained by generating continuous profiles of dated layers from high-resolution radar mapping of near-surface internal layers in the ice sheet (isochrones). To generate such profiles we designed and developed an ultrawideband radar for high-resolution mapping of internal layers in the top 200 m of ice and tested it at the North Greenland Ice Core Project drill site. Reflection profiles of 2- and 10-km length reveal horizons that we correlate with electrical conductivity measurement (ECM) recordings. Our results show that the radar-determined depth of internal layers is within ±2 m of that in an ice core collected at a nearby location. Preliminary frequency analyses of layer reflections reveal that the reflections are strongest at the 500–1000 MHz frequency range. Long-term accumulation rate computed from radar data is within 5% of that obtained from snow pits.

1. Introduction

Sea level has been rising at about 2 mm/yr over the last century. About half of this rise is attributed to thermal expansion of the ocean and melting of mountain glaciers [*Intergovernmental Panel on Climate Change* (*IPCC*), 1995]. To assess the role of the Antarctic and Greenland ice sheets in sea level rise, an improved knowledge of the mass balance of these ice sheets is required. There are two methods to determine the mass balance of an ice sheet. The first is the flux method, where a comparison is made between the (net) long-term average input (net accumulation) and output (ice flow) fluxes. The second is the volumetric method, where changes in surface elevation are measured. Clearly, along with ice velocities, ice thickness, surface temperature and topography, and ablation measurements, an accurate knowledge of accumulation rate is needed for the flux method, and interannual variability of snowfall is needed to interpret results from the volumetric method [*van der Veen and Bolzan*, 1999; *McConnell et al.*, this issue; *Davis et al.*, 2000].

Currently, accumulation information is determined from ice cores and pits [*Patterson*, 1994]. *Ohmura and Reeh* [1991] generated an accumulation map using data on 251 pits and cores and precipitation measurements from 35 meteorological stations located in the coastal regions. The accuracy of this map is clearly a function of the spatial location of the data points. *Ohmura and Reeh* [1991] also reported that an inherent accumulation rate uncertainty of 20% in their map was due to the inconsistency between the meteorological precipitation and the glaciologically determined accumulation. In addition, more than 75 different cores from 50 distinct locations were obtained in the NASA PARCA program. Information from these cores was used to generate an updated map of accumulation over the Greenland ice sheet. *Bales et al.* [this issue] report that the uncertainty in accumulation is on the order of 24% at certain areas.

To provide improved spatial and temporal coverage, the development of remote sensing methods for estimating the accumulation rate is thus required. An accurate estimate of the long-term accumulation rate can be obtained by mapping a continuous profile of the dated layers in the ice sheet. The dated layers here refer to known volcanic and melt events. Volcanic events register as a change in conductivity [*Hammer*, 1980], whereas the melt events are marked by a change in the density. Reflection profiles from ice-sounding radar systems show many internal ice reflections between the bedrock and the surface, and the source of these internal reflections has been identified as layering involving small conductivity changes due to changes in acidity from large volcanic events [*Millar*, 1981]. By mapping shallow internal layers we will be able to identify known melt and volcanic events, and this information, combined with published density and thickness data, can be used to estimate the accumulation rate over a range of time periods. Also, we can reduce the errors due to local variability, as well as study the effect of such local variability by collecting information on the near-surface layers over distances greater than several ice thicknesses.

Although there are several types of radar systems that can measure the thickness of the ice sheet, there appears to be no system capable of achieving less than 1 m vertical resolution to 200-m depth, which is needed to map internal layers for accumulation estimation. To determine the optimum radar parameters for this, we performed simple simulations on ice sheet models. The electrical conductivity measurements of ice cores and published real value of permittivity were used to model the electrical properties of the ice sheet. The finite-difference time-domain (FDTD) [*Yee*, 1966] technique was then used on the ice model to determine the optimum radar parameters by simulating the scattering response of the ice sheet due to radar sounding. We then designed an ultrawideband frequency-

[1]Now at Department of Glaciology, University of Copenhagen, Copenhagen, Denmark.

Paper number 2001JD900191.
0148-0227/01/2001JD900191$09.00

modulated-continuous-wave (FMCW) radar system [*Saunders*, 1990; *Stove*, 1992] to operate over the frequency range from 170 to 2000 MHz for imaging the top 200–300 m of ice with high vertical resolution on the order of 0.5 m. We performed shallow radar-sounding experiments at the North Greenland Ice Core Project (NGRIP) site (75.1°N, 42.3°W) during June and July 1998 and in August 1999. We collected data over a 2-km and a 10-km traverse with the radar mounted on a tracked vehicle.

To date, FMCW radar has only been used for shallow snow and ice soundings [*Boyne and Ellerbruch*, 1979; *Yankielun et al.*, 1992; *Arcone et al.*, 1997; *Koh et al.*, 1996; *Richardson et al.*, 1997; *Holmgren et al.*, 1998] at frequencies ranging from 800 to 12 GHz and for soundings to 60 m in temperate ice at 1–2 GHz [*Arcone and Yankielun*, 2001]. Our system greatly improves the FMCW radar performance and demonstrates the stratigraphic resolution possible.

2. Background

Fujita et al. [2000] have reported that the complex permittivity of the ice sheet is a function of crystal orientation fabrics, density, impurities (acidity concentration), and temperature. Vertical discontinuities in the crystal orientation fabric have been detected at Dome Fuji, East Antarctica. Even though these discontinuities are only a few centimeters thick, they produce strong radar reflections. The amplitude of the reflection coefficient caused by changes in crystal orientation fabric is independent of ice temperature and frequency [*Fujita et al.*, 2000].

Density changes are primarily caused by melt events. The formation of a high-density melt layer occurs when a layer of snow or near-surface firn melts during the summer and the drainage forms a layer that subsequently refreezes. In between the winter and the summer seasons a new layer of snow accumulates over the melt layer. Hence the melt layer is sandwiched between two layers of low-density snow or firn. Density changes seen in the dry snow zone are primarily due to the pressure exerted by accumulation of snow above a layer. A transmitted radar signal will reflect from the interfaces between these layers due to the contrasts in the dielectric constant, which is proportional to density. A relationship between the dielectric constant and density is presented in section 6.1, where the wave speed due to firn density is computed. For a monochromatic wave, the reflection coefficient for a three-layer media, Γ, at a firn interface of an embedded layer is given by

$$\Gamma = \frac{\sqrt{\varepsilon_{r2}} - \sqrt{\varepsilon_{r1}}}{\sqrt{\varepsilon_{r2}} + \sqrt{\varepsilon_{r1}}} 2 \sin\left(\frac{2\pi l}{\lambda_m}\right), \quad (1)$$

where ε_{r1} is the dielectric constant of layer 1 and layer 3, ε_{r2} is the dielectric constant of layer 2, l is the thickness of layer 2, and λ_m is the wavelength in layer 2.

The magnitude of the reflection coefficient increases as the dielectric contrast increases, but it is modulated by a sinusoidal term related to layer thickness and wavelength. The maximum value of the reflection coefficient occurs whenever layer thickness is an odd integer multiple of $\lambda_m/4$. The real part of the dielectric constant does not vary as a function of frequency or temperature [*Fujita et al.*, 2000].

Variations in conductivity have also been shown to be sources of internal reflections [*Hammer*, 1980; *Fujita and Mae*, 1994]. These variations are due to the acidic impurities embedded in the ice during volcanic eruptions. We derive below the reflection coefficient due to a change in conductivity.

The permittivity of the background and acidic layer can be expressed as

$$\varepsilon_{r1} = \varepsilon'_{r1} - j\varepsilon''_{r1} \quad (2)$$

$$\varepsilon_{r2} = \varepsilon'_{r2} - j\varepsilon''_{r2}, \quad (3)$$

where ε_{r1} is the dielectric constant of the background, and ε_{r2} is the dielectric constant of the acidic layer.

Let us assume that $\varepsilon''_r/\varepsilon'_r \ll 1$, and $\varepsilon'_{r1} = \varepsilon'_{r2}$. The reflection coefficient from an acidic layer can be written as

$$\Gamma = \frac{\sqrt{\varepsilon_{r2}} - \sqrt{\varepsilon_{r1}}}{\sqrt{\varepsilon_{r2}} + \sqrt{\varepsilon_{r1}}} 2 \sin\left(\frac{2\pi l}{\lambda_m}\right), \quad (4)$$

where $\sqrt{\varepsilon_{r2}} = \sqrt{\varepsilon'_{r2} - j\varepsilon''_{r2}}$.

Using the above assumptions,

$$\sqrt{\varepsilon_{r2}} \approx \sqrt{\varepsilon'_{r2}} - \frac{j\varepsilon''_{r2}}{2\sqrt{\varepsilon'_{r2}}}. \quad (5)$$

Similarly,

$$\sqrt{\varepsilon_{r1}} \approx \sqrt{\varepsilon'_{r1}} - \frac{j\varepsilon''_{r1}}{2\sqrt{\varepsilon'_{r1}}}. \quad (6)$$

Equation (4) can then be simplified to

$$\Gamma \approx \left|\frac{(\varepsilon''_{r1} - \varepsilon''_{r2})}{4\varepsilon'_{r2}}\right| \exp\left(j\frac{\pi}{2}\right) 2 \sin\left(\frac{2\pi l}{\lambda_m}\right). \quad (7)$$

The equation above shows that the reflection coefficient due to a conductive change can be approximated with an imaginary quantity. However, *Fujita et al.* [2000] have shown that the phase delay of the reflection coefficient drops below $\pi/2$ with increasing frequency for temperatures above the eutectic point of the acid. Thus there is a contribution from the real part of the dielectric constant as well for temperatures above the eutectic point. The contribution to the real part of the reflection coefficient is probably due to the presence of liquid associated with impurities in the volcanic layer [*Fujita et al.*, 2000] which may be present for temperatures above −40°C.

3. Simulation

We performed a finite-difference time-domain (FDTD) simulation to determine the radar sensitivity required to map shallow internal layers. We used the electrical conductivity data from the GRIP core [*Clausen et al.*, 1995] to estimate the imaginary part of the complex permittivity required for our simulation. We assumed that the permittivity is constant as a function of depth for our simulations. We used a relative permittivity of 2 and a conductivity of 17 μS/m for the ice sheet. The volcanic ash embedded in the ice sheet was modeled as a layer with a relative permittivity of 2 and a conductivity of 40 μS/m. Using this information, we computed the shape of a radiated 2-GHz, 1000-V peak-to-peak pulse transmitted through and reflected from a 5-cm layer of acidic volcanic ash. Figure 1 shows the dielectric profile used in our simulation on the left and the simulation results on the right. In the figure on the right the first peak is the return from air-firn interface, and the second peak is the return from the volcanic layer located at

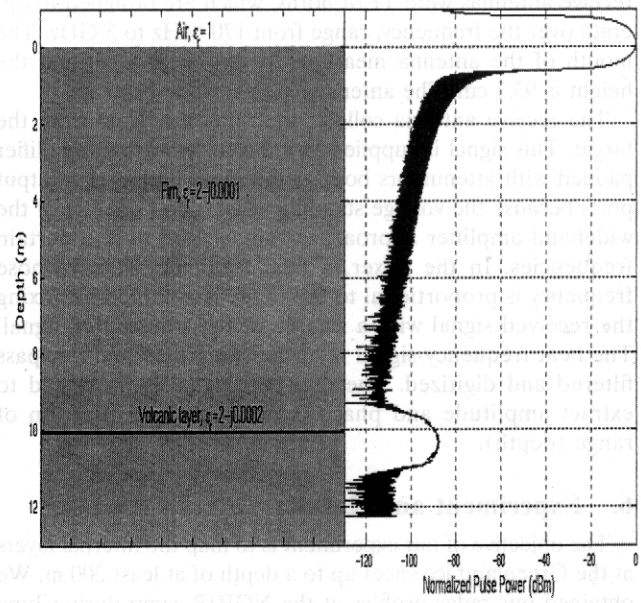

Figure 1. Dielectric profile used in our simulation (left) and the finite-difference time-domain (FDTD) simulation results (right).

a depth of 10 m below the air-firn interface. The return from the volcanic layer is about 85 dB below that from the air-firn interface. Because higher frequencies are attenuated as the signal propagates through the medium, the 3-db pulse width of the return from the volcanic layer is about 1.1 times wider than that from the air-firn interface.

The simulation shows that our system will require a dynamic range of at least 85 dB if we were to operate the system at 2 GHz. Since we are using a 12-bit digitizer with a dynamic range of 72 dB, we will have to attenuate the reflection from the air-ice interface by at least 13 dB relative to the weak reflections from the internal layers. The dynamic range requirement would be less stringent for systems operating at a lower frequency since the amplitude of the reflection coefficient due to conductivity changes increases with decreasing frequency. On the basis of simulation results we decided to build a frequency-modulated continuous-wave (FMCW) radar operating over the frequency range from 200 to 2000 MHz. Range gating is easy to implement in an FMCW radar with filters as opposed to the very fast switches required in a short-pulse radar. For this reason we built an ultrawideband FMCW radar for our exploratory surface-based measurements. The energy reflected by shallow internal layers at frequencies higher than about 1 GHz is small. We used bandwidth in excess of that required to provide range resolution of 50 cm (~450 MHz with the Hanning weighting function) to minimize the effect of range sidelobes of the strong surface reflection.

4. Principles of FMCW Radar Operation

As opposed to short-pulse radar, which transmits a 2–3 cycle oscillation, an FMCW radar repetitively transmits a waveform in which the frequency continually increases. The waveform is modulated over a fixed bandwidth, which determines the range resolution; the larger the bandwidth, the higher the range resolution. The return signal from the target is then compared with the transmitted signal to extract the range, amplitude, and phase information of the target. The difference between the return signal and the transmitted signal is known as the intermediate frequency (IF) or beat signal.

The transmitted signal voltage $v_t(t)$ is given as

$$v_t(t) = A \cos (2\pi f_0 t + 2\pi B f_m t^2 + \theta_0), \tag{8}$$

where f_0 is the initial sweep frequency, B is the FM sweep bandwidth, f_m is the modulation frequency, θ_0 is the initial phase of the sweep source, and t is time.

Let us assume that the transmit signal impinges on a single volcanic layer and reflects back. The received signal at the receive antenna is

$$v_r(t) = A'\Gamma[f(t)] \cos \{2\pi f_0(t - \tau) + 2\pi B f_m(t - \tau)^2 + \theta_0 + \phi[f(t)]\}, \tag{9}$$

where τ is the time it takes for the signal to travel the two-way distance between the target and the radar, $\Gamma[f(t)]$ is the magnitude of the reflection coefficient of the volcanic layer, and $\phi[f(t)]$ is the phase of the reflection coefficient. The reflection coefficient is a function of the transmit signal frequency, $f(t)$, which as indicated is a function of time.

The received signal is down converted to IF by mixing it with a portion of the transmit signal. After filtering out the higher-order terms we obtain the following expression:

$$v_r(t) = A'\Gamma[f(t)] \cos \{2\pi f_0\tau + 2\pi B f_m \cdot (2\tau t - \tau^2) - \phi[f(t)]\}. \tag{10}$$

The above equation can be rewritten in terms of the beat frequency (or IF), f_b. The beat frequency is the instantaneous difference frequency between the transmitted and the received signal and is given by

$$f_b = 2\tau B f_m. \tag{11}$$

Substituting the above equation into (10), we obtain

$$v_r(t) = A'\Gamma[f(t)] \cos \{2\pi f_b t + 2\pi f_0\tau - \pi f_b\tau - \phi[f(t)]\}. \tag{12}$$

The amplitude and phase of the target's reflection coefficient can be extracted by means of the Hilbert transform (HT) of the IF signal above. The HT of the IF signal will give us a complex signal in the following form:

$$v_r(t) = A'\Gamma[f(t)] \exp (j\{2\pi f_b t + 2\pi f_0\tau - \pi f_b\tau - \phi[f(t)]\}). \tag{13}$$

We can obtain the phase response of the target by computing the phase term in (13), removing the range contribution in the phase term and then calibrating it with a target of known phase. The amplitude can be similarly obtained by computing the magnitude of the complex signal and calibrating it with a target of known amplitude. Figure 2 shows the results of the amplitude and phase extraction technique on simulated radar data. The recovered signal is almost identical to the simulated response except at the edges where there is a slight ringing. The simulation was not on any real target, because the purpose of the simulation was to show that it is possible to recover the reflection profile of a target.

5. System Description

Figure 3 diagrams our FMCW radar system. We used a triangular voltage waveform at the control port of a YIG os-

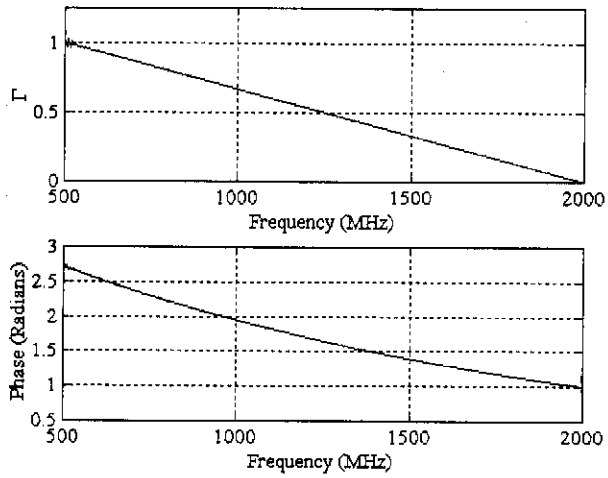

Figure 2. Amplitude and phase extraction using simulated radar data.

cillator to generate a transmit signal whose frequency increases linearly with applied voltage during the upsweep and decreases linearly during the downsweep. The triangular waveform is digitally generated and converted to an analog signal on a PCI card that is housed in the host computer. A DC- to 2-GHz sweep is generated by down converting a 4- to 6-GHz chirp from the YIG oscillator using a 4-GHz phase-locked signal. The frequency of operation can be varied within this bandwidth via the computer. We operated our system from 170 MHz to 2 GHz since the cutoff frequency of the antenna at the lower end is 170 MHz. The variable-gain amplifier enables us to set the output power to a constant level. The amplifier output is supplied to the transmit antenna through a coupler, an attenuator, and a power amplifier, which increases the signal level to about 23 dB m. The coupler is used to derive a sample of the transmit signal to serve as a local oscillator. The attenuator minimizes multiple reflections between the amplifier input and the coupler output ports. The transmit and receive antennas were TEM horns, which are designed to operate over the frequency, range from 170 MHz to 3 GHz. The mouth of the antenna measures 94 cm by 68.6 cm and the height is 93.3 cm. The antennas are shown in Plate 2a.

The receive antenna collects the reflected signal from the target. This signal is supplied to a mixer through an amplifier padded with attenuators both at the input and at the output ports because the voltage standing wave ratio (VSWR) of the wideband amplifier approaches values close to 2 at certain frequencies. In the mixer, a beat frequency signal whose frequency is proportional to the range is obtained by mixing the received signal with a sample of the transmitter signal. The beat frequency signal is further amplified and low-pass filtered and digitized. The digitized signal is processed to extract amplitude and phase information as a function of range (depth).

6. Experiment and Results

The objective of our experiment is to map the internal layers at the Greenland ice sheet up to a depth of at least 200 m. We obtained our radar profiles at the NGRIP camp during June and July 1998 and August 1999. The NGRIP camp is located 3000 m above sea level in the middle of the Greenland ice cap at 75.1°N, 42.3°W (Plate 1). We mounted the radar on a tracked vehicle (Trackmaster) and collected data over a 2-km transect in 1998 and a 10-km transect in 1999. The antennas were mounted on both sides of the Trackmaster as shown in Plate 2a. The apertures of the antennas were about 2 m above the snow surface. The radar and data acquisition systems were mounted in a Hardigg box as shown in Plate 2b. The systems were powered by a portable generator that was regulated using an uninterruptible power supply (UPS). The Trackmaster was operated at a speed of about 6.7 ms^{-1} (24 kph) during our measurements. The pulse repetition frequency (PRF) of the transmitted RF signal was 8 Hz. The IF signal (echo trace) was sampled at 1 MHz and digitized using a 12-bit A/D card [*Akins*, 1999]. Eight traces were coherently integrated before storage.

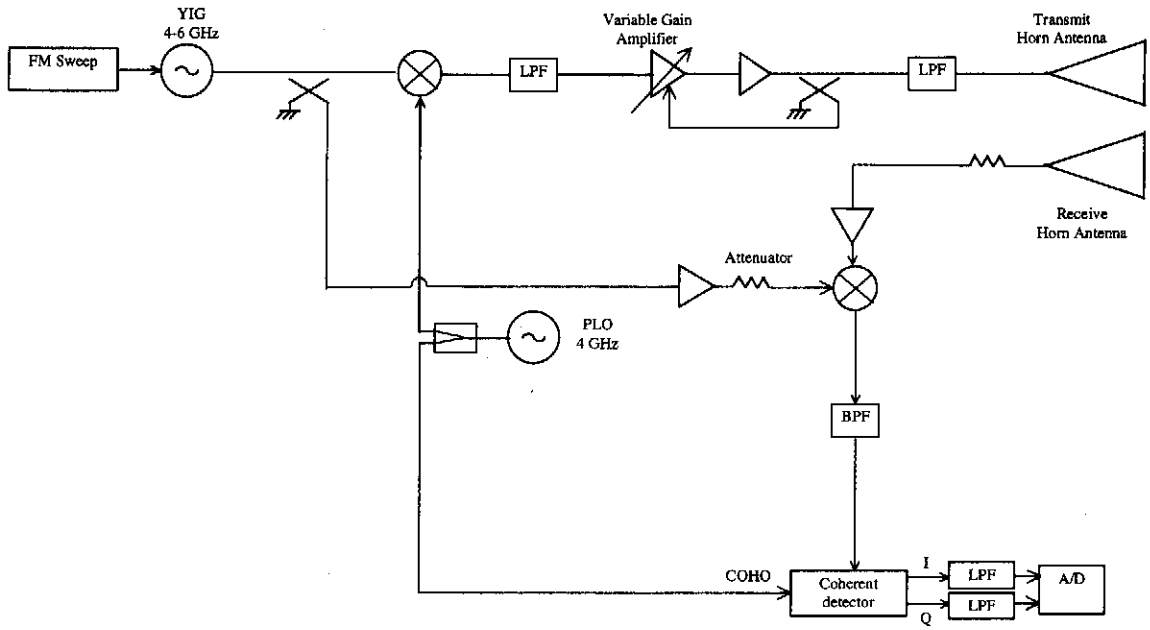

Figure 3. Block diagram of the prototype wideband FMCW radar system for mapping internal layers.

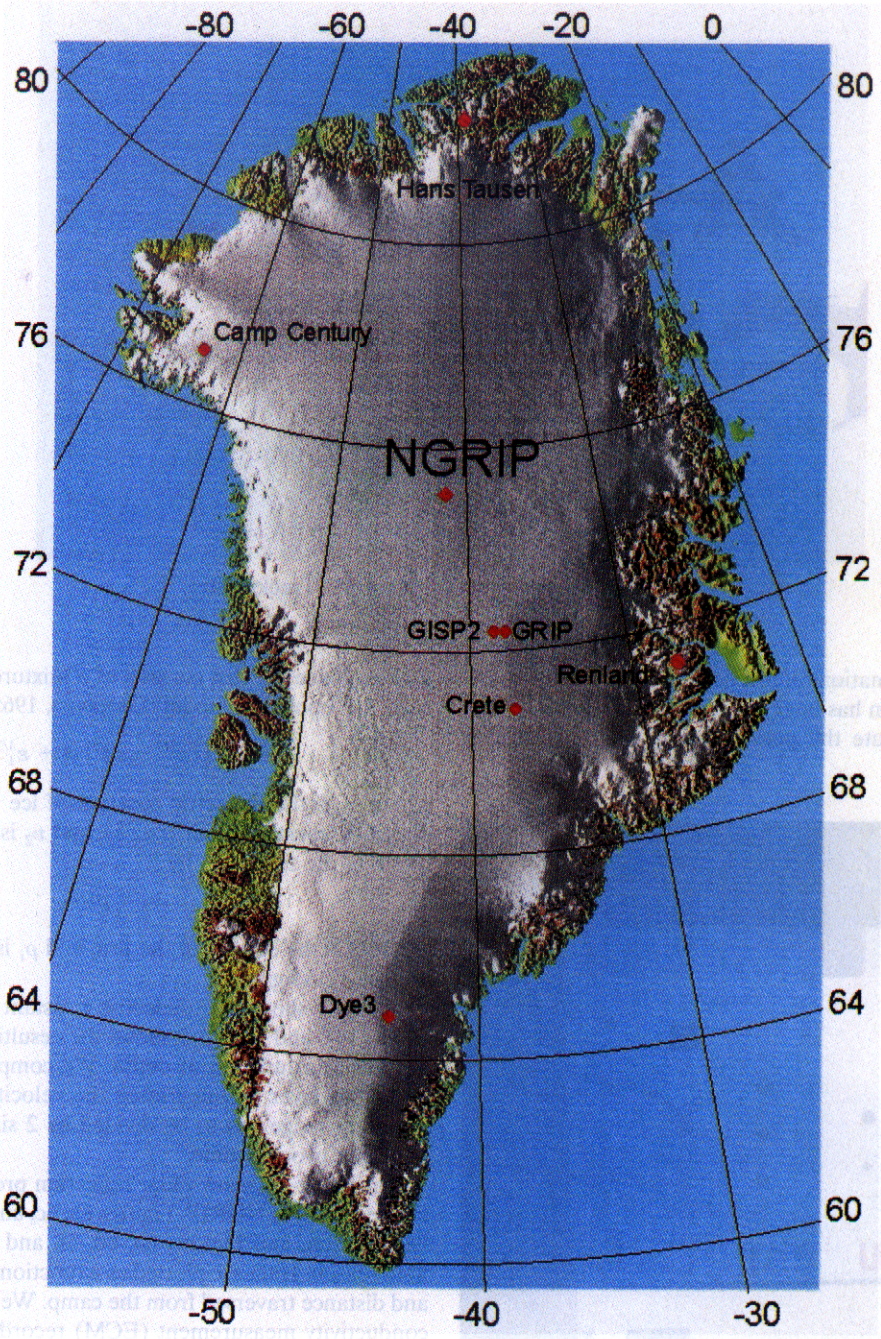

Plate 1. Location of the North Greenland Ice Core Project (NGRIP) site.

During postprocessing in the laboratory, we removed the DC offset in the time series data, applied a Hanning window to reduce the range sidelobes in the frequency domain, and Fourier transformed the windowed data to obtain spectral plots. We then low-pass filtered the spectral data to determine the amount of gain needed to correct for the $1/r^2$ power falloff with range because we used a high-pass filter to attenuate the strong surface reflections to match the dynamic range of the received signal to the A/D converter. The original spectra were then multiplied with the inverse of the low-pass-filtered data to obtain the gain-corrected spectra. The gain correction was applied from about 10 m since the transition band of the high-pass filter occurs after this range. The gain correction could not be applied before this range because the signals were too small to be inverted accurately in the stop band of the high-pass filter. All the spectra along the traverse were compiled to produce a reflection profile for the transect, and then median filtering was applied along the layers to smooth the image.

6.1. Results

Glacial ice and firn, particularly in the top 200 m, are stratified media. The density, and therefore the velocity of propagation, varies with depth. Therefore to determine the thickness of layers between two events from a measured range, we must

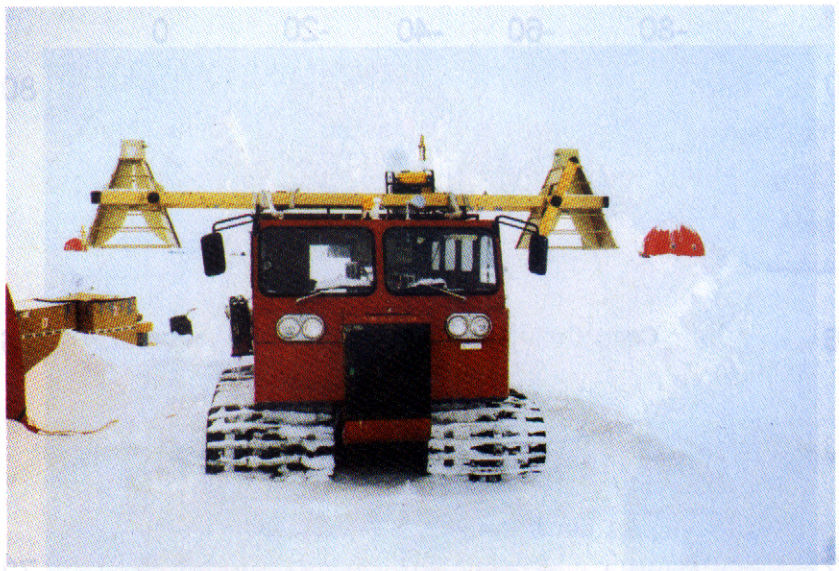

Plate 2a. Antennas mounted on the Trackmaster.

have additional information on firn density. The density of firn up to a depth of 275 m has been measured at the NGRIP site.

We need to compute the permittivity of a heterogeneous mixture since the firn consists of a mixture of air and ice. We used the Looyenga model [*Looyenga*, 1965] given by

$$\varepsilon = [(\varepsilon_2^{1/3} - \varepsilon_1^{1/3})v_2 + \varepsilon_1^{1/3}]^3, \tag{14}$$

where ε_2 is the dielectric constant of ice (i.e., 3.15), ε_1 is the dielectric constant of air (i.e., 1), and v_2 is the volume fraction of ice in the firn given by

$$v_2 = \rho/\rho_i, \tag{15}$$

where ρ is the density of the firn, and ρ_i is the density of pure ice (i.e., 918 kg/m^3).

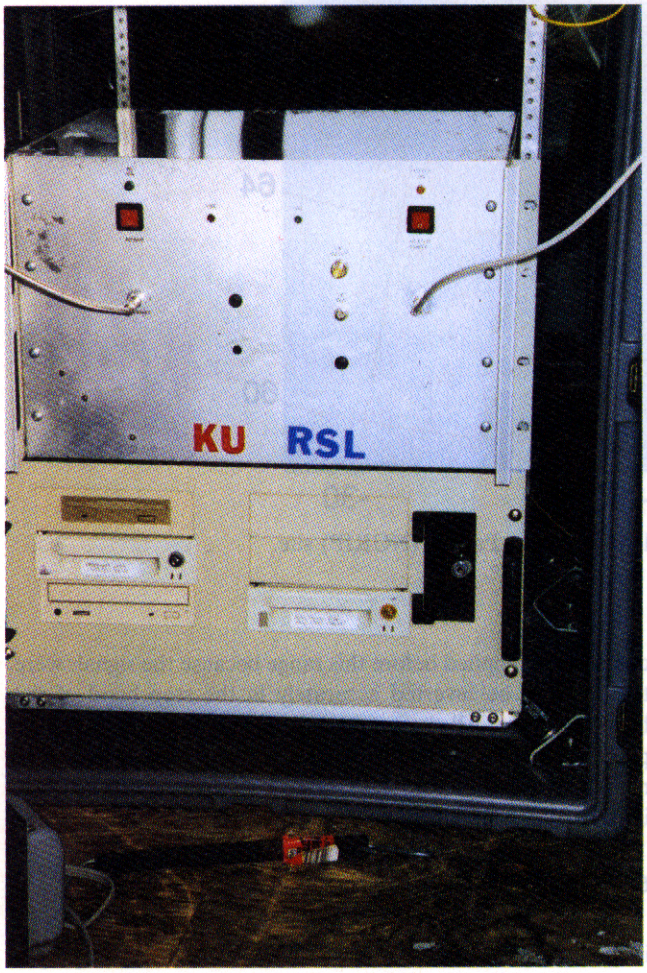

Plate 2b. (top) Radar system and (bottom) data-acquisition computer mounted in a Hardigg box in the Trackmaster.

Figure 4 shows the dielectric constant that was computed using (14), and Figure 5 shows the resulting velocity of propagation as a function of depth. We computed the range to a particular layer by integrating the velocity curve. The corresponding range has to be divided by 2 since the time on the scale is a two-way time.

Figures 6a–6g show radar reflection profiles of internal layers, recorded at NGRIP. Figures 6a, 6c, and 6e are for the 1998 field season, and Figures 6b, 6d, 6f, and 6g are for the 1999 field season. Data are plotted as a function of depth into the ice and distance traversed from the camp. We placed the electrical conductivity measurement (ECM) records to the right of the figures for comparison with the layers detected by the radar. The depths for the 1998 and 1999 data were plotted on the same scale for comparison. We currently do not have high-resolution density data for comparison with the reflection profile; hence we are unable to account for all the reflections. Some of the weaker ECM peaks do not have a corresponding radar horizon, but the change in conductivity may be too low for the radar to detect. However, the multitude of radar horizons assures that one will always correspond with a major ECM peak.

Figures 6a and 6b show layers detected from the surface to a depth of 45 m. In these figures there are two layers detected by our system that match impurities at 25 m deposited during the Katmai eruption in 1912 and a melt event in 1889 at 34 m. There is also a strong reflection from a depth of 40 m, but this layer has yet to be identified.

Figures 6c and 6d show layers detected from depths of 45–

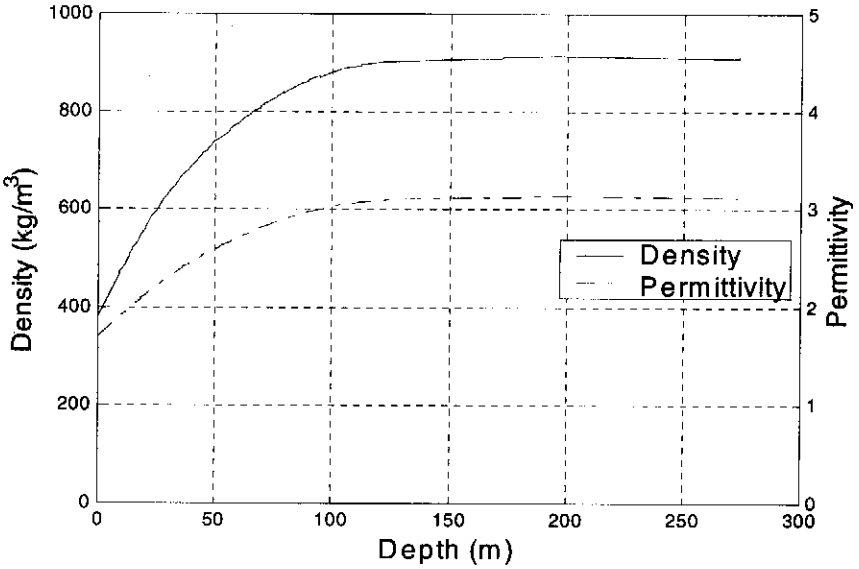

Figure 4. Density and permittivity of firn at NGRIP.

105 m. Here we have another two layers that have been identified as those resulting from the Tambora volcanic event in 1816 at 55 m and the Laki volcanic event in 1783 at 60 m (H. B. Clausen, personal communication, 1998).

Figures 6e and 6f show layers at depths between 105 m and 165 m. According to the density profile (Figure 4), this depth range and below is well within the ice region where density contrasts should be minimal. These two layers we believe are due to an unknown volcanic event in 1514 at 113 m and the Mount St. Helens volcanic event in 1479 at 118 m. Figure 6g shows layers that were detected between 165 m and 290 m during the 1999 experiment.

Table 1 shows the error between the radar-measured depths of major events and the depths determined from ice cores. This table shows that our errors are within ±2 m of the core-determined depths.

It has been reported in a previous study [*Fujita et al.*, 1999] that the reflections from the firn are due to the changes in the density. However, in this study the data were obtained with systems that have resolution of about tens of meters. With a resolution of this magnitude it will be difficult to resolve the weak reflections due to conductivity changes from the reflections due to density changes. However, we believe we are able to resolve the reflections with our high-resolution system. We are awaiting high-resolution density data to verify this.

We analyzed the data to determine the frequency response of the signal reflected by some of the layers. The frequency response of the layer was determined by taking the IFFT of the

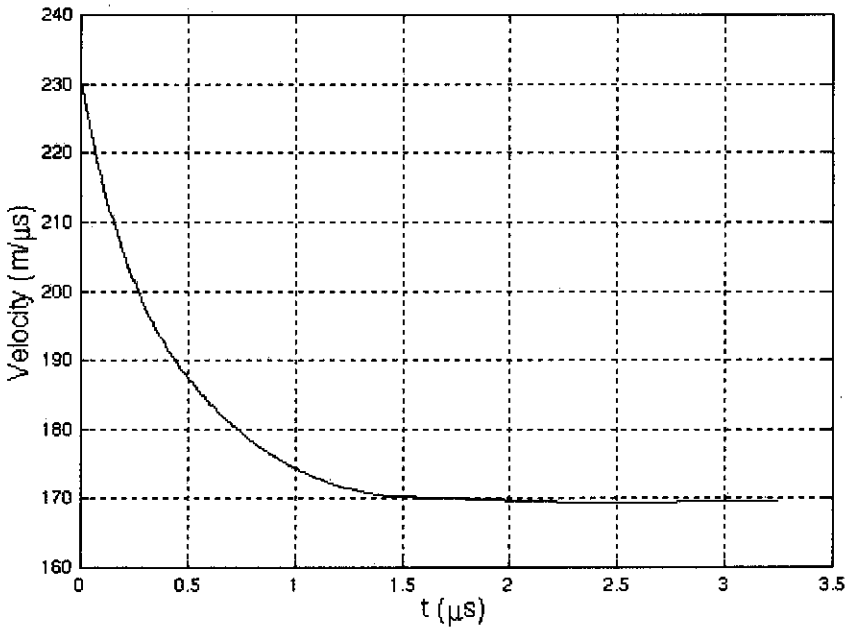

Figure 5. Speed of radio wave in the firn.

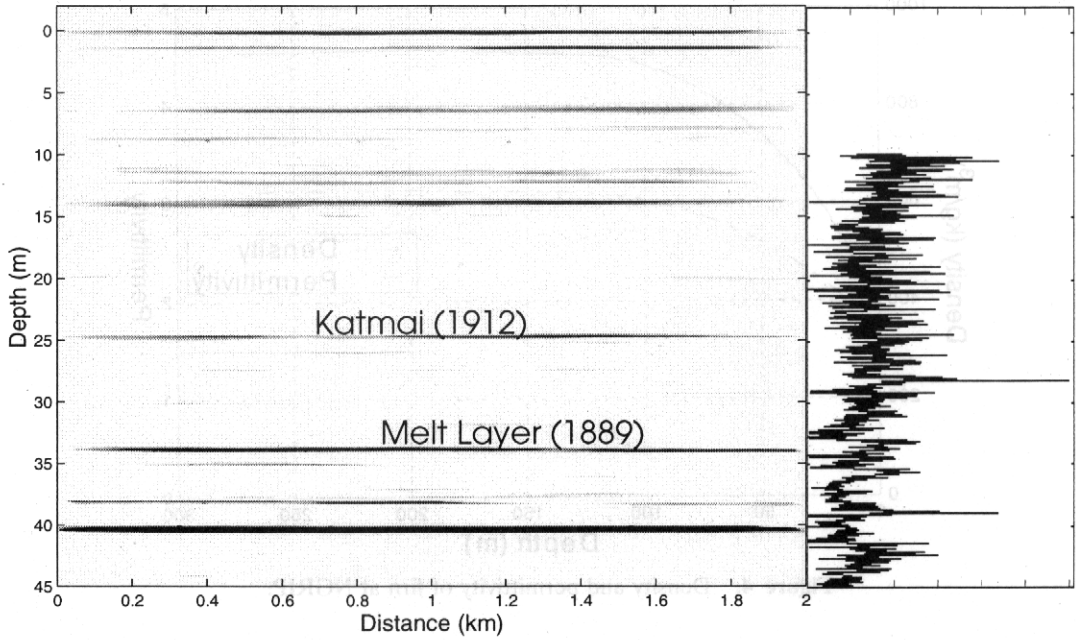

Figure 6a. Radar echogram of internal layers observed along a 2-km transect at NGRIP in 1998 (0–45 m depth).

filtered layer return and calibrating it with respect to the return from a metal plate. We used computed wave speed in the firn to estimate range to the layer. Figure 7 shows the frequency response of the reflection from the layer located at about 148 m. This result indicates that most of the contribution to the layer reflection is due to the signal in the 500–1000 MHz range.

The layer depths measured with our radar are within ±2 m of the layers obtained from ice core data. We did not adjust the density profile to match radar-determined depths with core data. Using the radar data from the 1998 and 1999 experiments and neglecting the effect of creep, we computed the average accumulation rate from radar-determined depths and density data from the NGRIP core as

$$\text{Accumulation rate, } A = \frac{dR}{dt}\frac{\rho_{\text{layer}}}{\rho_{\text{water}}}, \tag{16}$$

where dR/dt is the change in thickness over time, ρ_{layer} is the average density between the two layers, and ρ_{water} is the density of water.

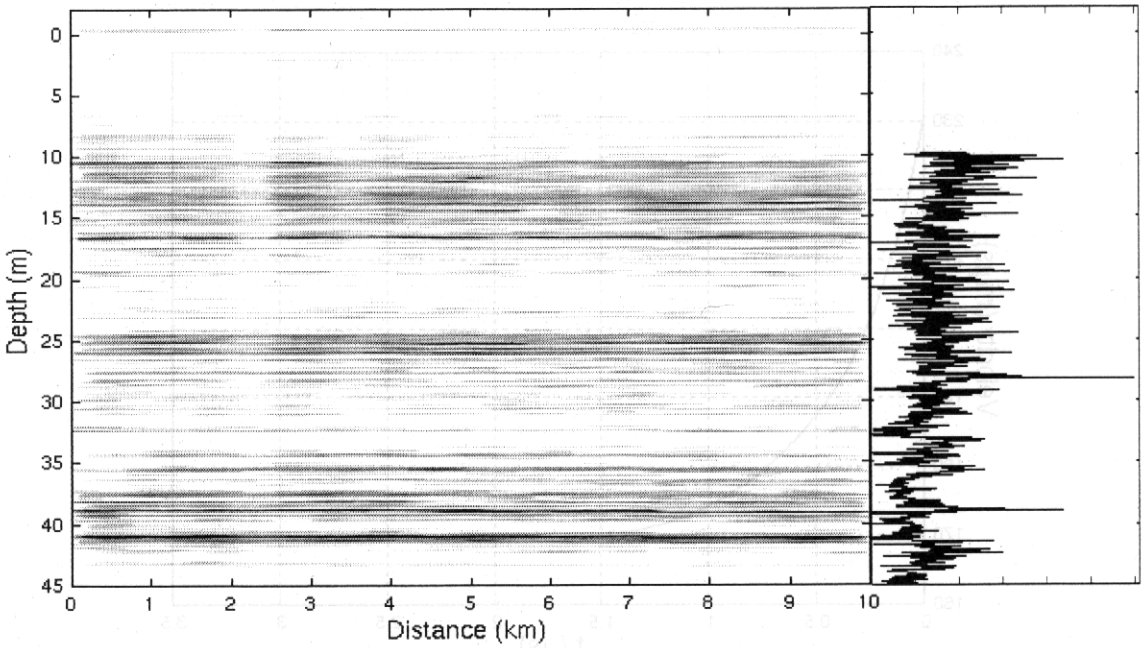

Figure 6b. Radar echogram of internal layers observed along a 10-km transect at NGRIP in 1999 (0–45 m depth).

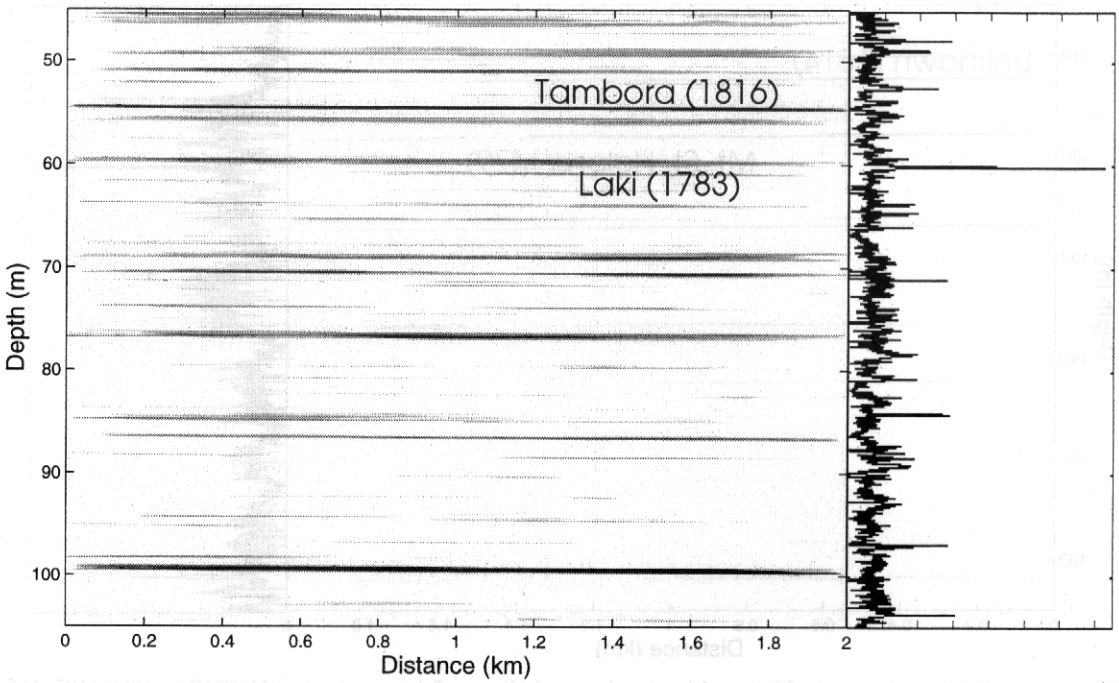

Figure 6c. Radar echogram of internal layers observed along a 2-km transect at NGRIP in 1998 (45–105 m depth).

To determine the error in our accumulation rate computation, we will first have to compute the uncertainty in our range computation. The range is computed using the following equation:

$$R = \frac{c\tau}{2\sqrt{\varepsilon}}. \tag{17}$$

The uncertainty in the range σ_R is related to the uncertainty in dielectric constant σ_ε and is given by

$$\sigma_R = \sigma_\varepsilon \frac{\partial R}{\partial \varepsilon}, \tag{18}$$

where

$$\frac{\partial R}{\partial \varepsilon} = -\frac{R}{2\varepsilon}. \tag{19}$$

The uncertainty in the dielectric constant is related to the uncertainty in the density σ_ρ and is given by

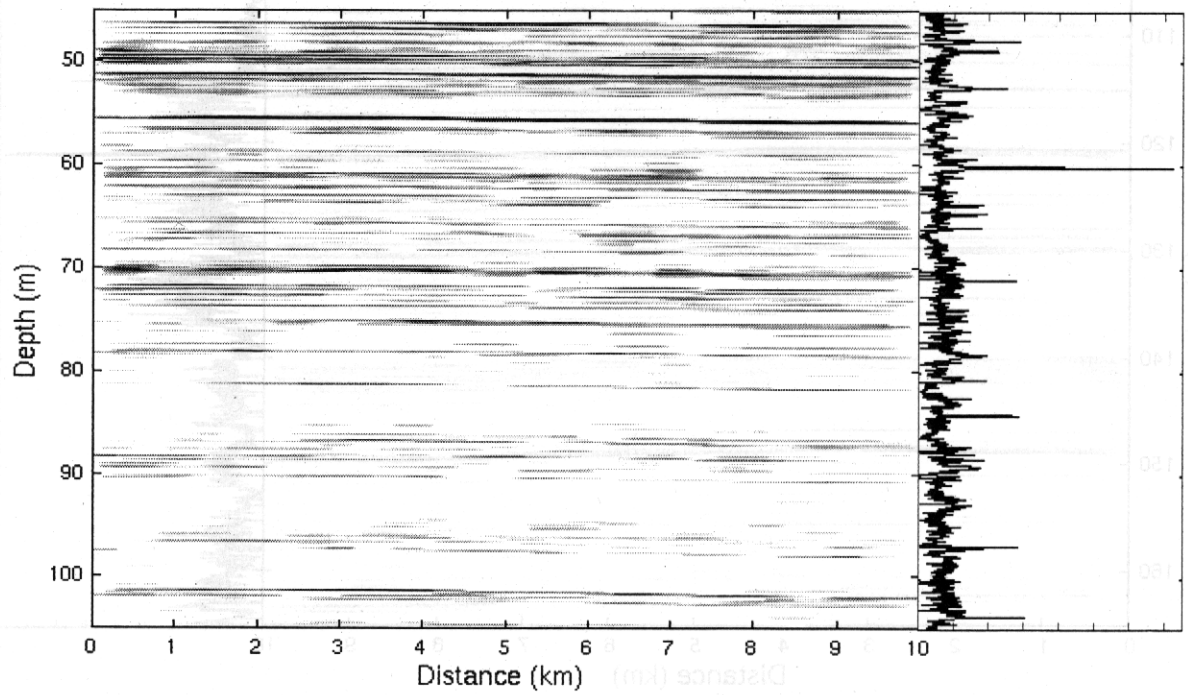

Figure 6d. Radar echogram of internal layers observed along a 10-km transect at NGRIP in 1999 (45–105 m depth).

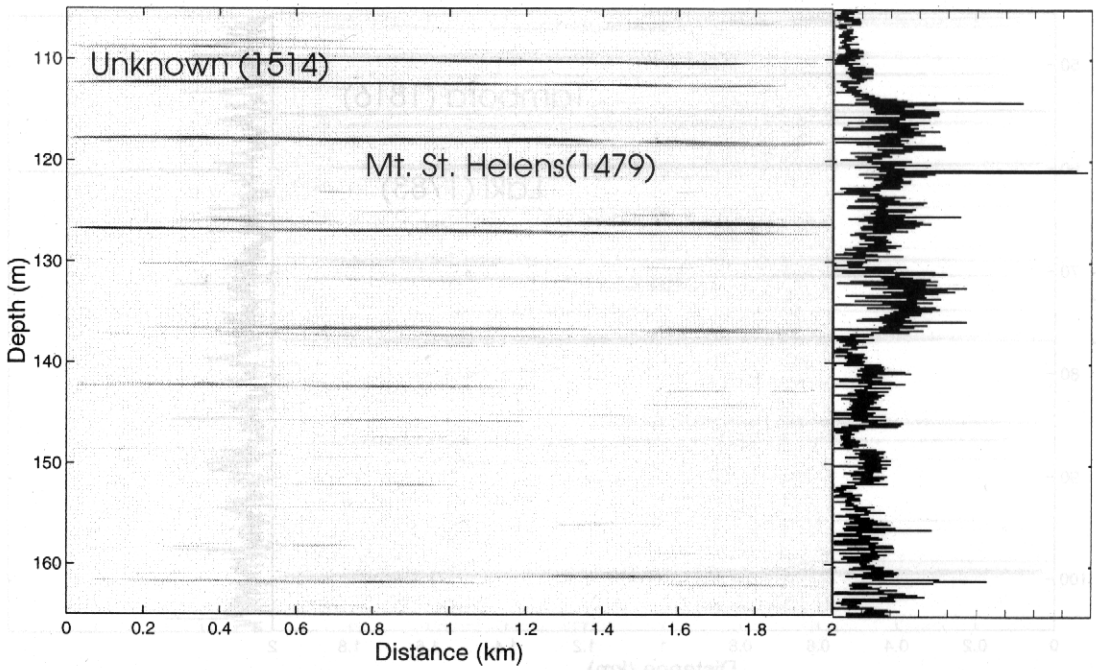

Figure 6e. Radar echogram of internal layers observed along a 2-km transect at NGRIP in 1998 (105–165 m depth).

$$\sigma_\varepsilon = \sigma_\rho \frac{\partial \varepsilon}{\partial \rho}, \tag{20}$$

where

$$\frac{\partial \varepsilon}{\partial \rho} = 3\left[(\varepsilon_2^{1/3} - \varepsilon_1^{1/3}) \frac{\rho}{\rho_i} + \varepsilon_1^{1/3} \right]^2 \left[\frac{(\varepsilon_2^{1/3} - \varepsilon_1^{1/3})}{\rho_i} \right], \tag{21}$$

hence

$$\sigma_\varepsilon = \sigma_\rho 3\left[(\varepsilon_2^{1/3} - \varepsilon_1^{1/3}) \frac{\rho}{\rho_i} + \varepsilon_1^{1/3} \right]^2 \left[\frac{(\varepsilon_2^{1/3} - \varepsilon_1^{1/3})}{\rho_i} \right]. \tag{22}$$

Substituting (21) and (22) into (18), we obtain the error expression for our range computation as

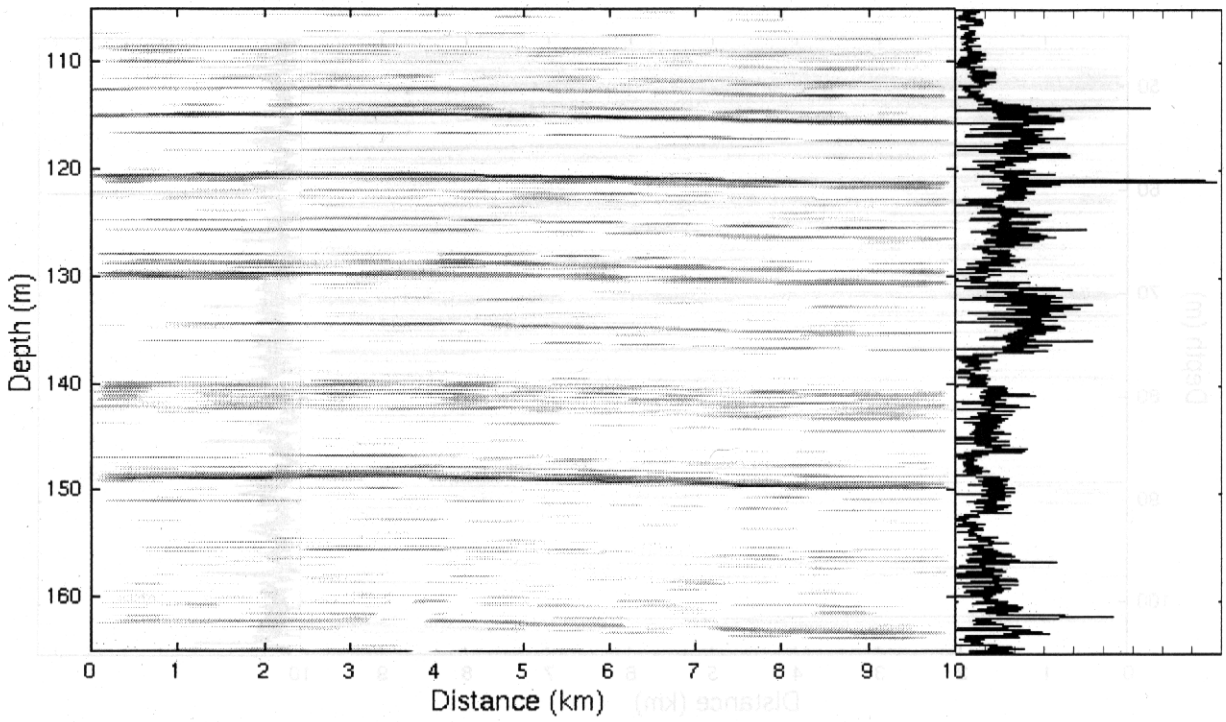

Figure 6f. Radar echogram of internal layers observed along a 10-km transect at NGRIP in 1999 (105–165 m depth).

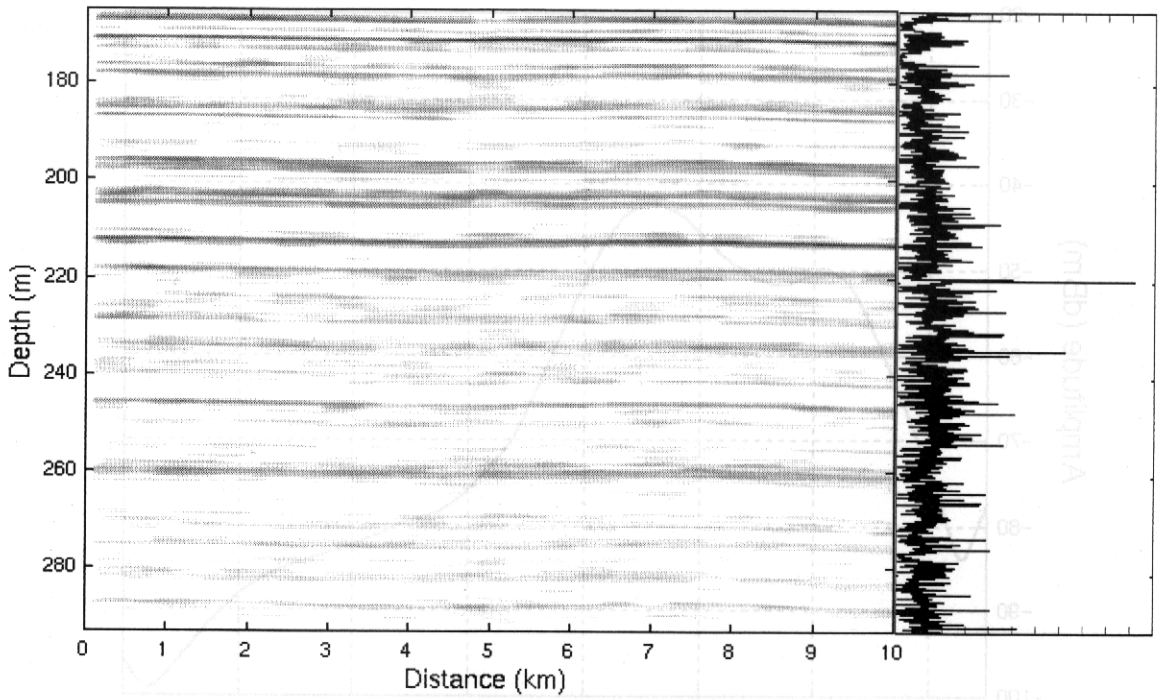

Figure 6g. Radar echogram of internal layers observed along a 10-km transect at NGRIP in 1999 (165–290 m depth).

$$\sigma_R = \frac{-\sigma_\rho 3R\left[\dfrac{(\varepsilon_2^{1/3} - \varepsilon_1^{1/3})}{\rho_i}\right]}{2\left[(\varepsilon_2^{1/3} - \varepsilon_1^{1/3})\dfrac{\rho}{\rho_i} + \varepsilon_1^{1/3}\right]}. \quad (23)$$

In addition to the error in the range due to uncertainty in the density, the range computation also depends on the resolution of the radar. Although we transmitted a 2-GHz-bandwidth signal, the frequency response of a typical reflection from the internal layer (Figure 7) shows a 10-dB bandwidth of 500 MHz. This translates to a ±30 cm uncertainty in the range. Hence the overall uncertainty in the range computation would be

$$\sigma_R = \frac{-\sigma_\rho 3R\left[\dfrac{(\varepsilon_2^{1/3} - \varepsilon_1^{1/3})}{\rho_i}\right]}{2\left[(\varepsilon_2^{1/3} - \varepsilon_1^{1/3})\dfrac{\rho}{\rho_i} + \varepsilon_1^{1/3}\right]} \pm 0.3, \quad (24)$$

where σ_ρ, the uncertainty in the density measurement, is 5%. This result can then be used to compute the uncertainty in the accumulation rate. The uncertainty in accumulation rate σ_A is given by

$$\sigma_A = \sqrt{\left(\sigma_R \frac{\partial A}{\partial R}\right)^2 + \left(\sigma_\rho \frac{\partial A}{\partial \rho_{\text{layer}}}\right)^2}, \quad (25)$$

where

$$\frac{\partial A}{\partial R} = \frac{\rho_{\text{layer}}}{t\rho_{\text{water}}}, \quad \frac{\partial A}{\partial \rho_{\text{layer}}} = \frac{R}{t\rho_{\text{water}}}.$$

Equation (25) becomes

$$\sigma_A = \sqrt{\left(\sigma_R \frac{\rho_{\text{layer}}}{t\rho_{\text{water}}}\right)^2 + \left(\sigma_\rho \frac{R}{t\rho_{\text{water}}}\right)^2}. \quad (26)$$

Tables 2a and 2b show the computed water-equivalent accumulation rate per year along with its uncertainty, over the periods indicated in column 1. The average density was determined by averaging the density of firn over the indicated period. The accumulation rate over this period is then calculated using (16). The average accumulation rate between 1259 and

Table 1. Depth Error Between Radar Data and Core Data

Event Year	Core Depth, m	Radar Depth 1998, m	Error 1998, m	Radar Depth 1999, m	Error 1999, m
1912	27	25	−2	25	−2
1889	34	34	0	35	1
1816	53	55	2	55	2
1783	59	60	1	61	2
1601	102	100	−2	102	0
1514	114	113	−1	115	1
1479	120	118	−2	120	0
1259	162	163	1	163	1

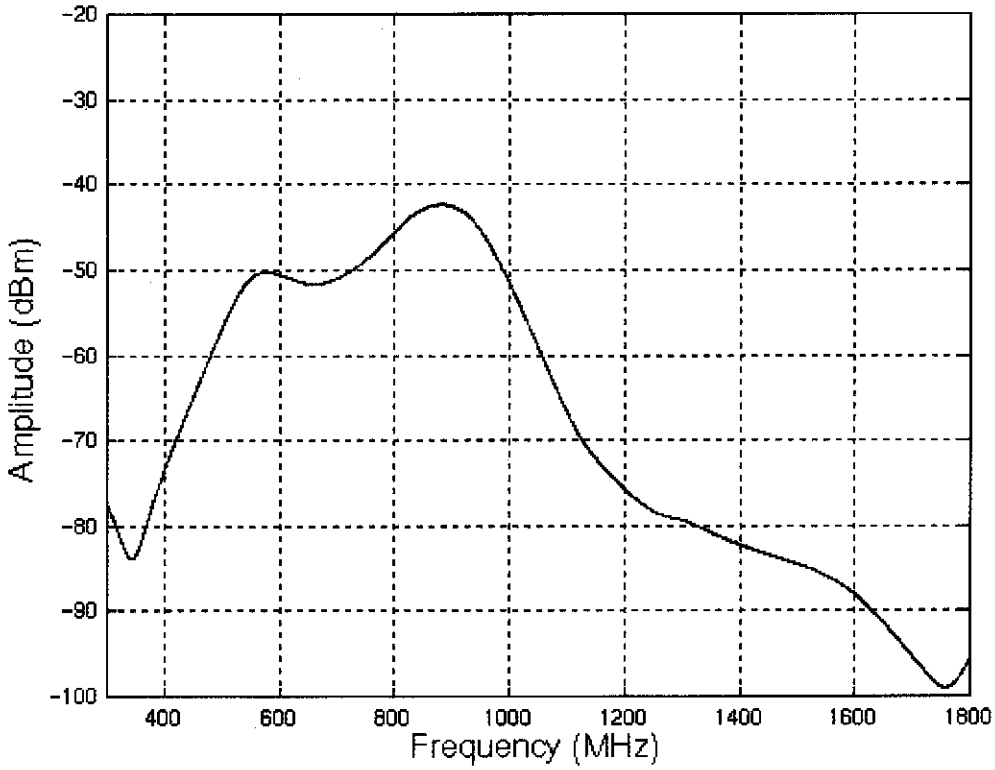

Figure 7. Frequency response of reflection from layer located at about 148 m.

1997 was determined by taking a weighted sum of the accumulation rate for each of the periods indicated in column 1 and dividing it by the total number of years over this period. Equation (26) was used to determine the uncertainty in the accumulation rate. The uncertainty over the entire period was determined by taking the square root of the sum of the squares of the uncertainty of the accumulation spanning this period; that is,

$$\sigma_A = \sqrt{\sigma^2_{A_{\text{layer1}}} + \sigma^2_{A_{\text{layer2}}} + \ldots + \sigma^2_{A_{\text{layerN}}}} \quad (27)$$

The average yearly rate between 1259 and 1997 was computed to be 17.3 cm/yr with an uncertainty of about 4%. *Dahl-Jensen et al.* [1997] report that modeling results indicate that the average snow accumulation rate is about 19 cm/yr. However, measurements at a location close to the NGRIP camp located at 75.0°N, 42.0°W indicate an accumulation rate of 17.1 cm/yr (S. Kipfstuhl, personal communication, 1998).

7. Summary and Future Directions

The accumulation rate is an important parameter required for mass balance computation of ice sheets. Previous accumulation rates were computed from the density of ice cores, and accumulation maps were drawn based on these sparse results [*Ohmura and Reeh*, 1991]. Some parts of this map have been shown to have about 20% errors. Many more cores have been drilled since then, and the accumulation rates have been computed more accurately by identifying the thickness between known volcanic events, which have deposited their acidic ash on the ice sheet [*Bales et al.*, this issue].

In this paper we present the design of a radar system to map near-surface internal layers in the Greenland ice sheet remotely. We developed a prototype ultrawideband FMCW radar system that operates from 170 to 2000 MHz based on some simple FDTD simulations of the volcanic-layer characteristics in the ice. We tested this system during the 1998 and 1999

Table 2a. Computed Accumulation Rate From 1998 Radar Data

	Measured Thickness, m	Average Density, g/cm^3	cm/yr	Percent Error
1912–1997	25	0.50	14.59	1.49
1889–1912	9	0.63	24.62	2.28
1816–1889	21	0.71	20.49	1.50
1783–1816	5	0.77	11.68	1.26
1601–1783	40	0.84	18.42	1.12
1514–1601	13	0.89	13.29	0.09
1479–1514	5	0.90	12.84	1.32
1259–1479	45	0.91	18.59	1.04
Mean			17.3	±4.01%

Table 2b. Computed Accumulation Rate From 1999 Radar Data

	Measured Thickness, m	Average Density, g/cm^3	cm/yr	Percent Error
1912–1997	25	0.50	14.59	1.49
1889–1912	10	0.63	27.49	2.47
1816–1889	20	0.71	19.59	1.43
1783–1816	6	0.77	14.05	1.35
1601–1783	41	0.84	18.96	1.14
1514–1601	13	0.89	13.33	0.87
1479–1514	5	0.90	12.87	1.32
1259–1479	43	0.91	17.76	0.99
Mean			17.3	±4.12%

NGRIP field seasons, and the results show that they are within ±2 m of the measured depths of the volcanic layers. The long-term accumulation rate computed from radar data is less than 5% of that obtained from snow pits.

This approach offers the potential for interpolating accumulation derived from sparse ice cores across any desired region of an ice sheet. However, this will only become practical if the surface-based radar techniques described here can be applied from an aircraft and integrated with in situ observations. On the basis of the results from our frequency analysis of the layer reflection we are developing an airborne FMCW radar that operates from 600 to 900 MHz for possible field deployment in the 2001 and 2002 time frame. We are designing this system to use synthetic aperture radar (SAR) in the along-track dimension and a large thinned array in the cross-track dimension to reduce antenna beam widths. With successful removal of off-vertical clutter we hope to obtain airborne data with as similar a high degree of certainty as with our ground-based system.

Acknowledgments. We would like to thank Steve Arcone and two anonymous reviewers for the valuable feedback that has helped improve the paper significantly. This work is supported by NASA grants NAG5-8758 and NGT5-50219.

References

Akins, T., Design and development of an improved data acquisition system for the coherent radar depth sounder, M.S. thesis, Electr. Eng. and Comput. Sci., Univ. of Kansas, Lawrence, Kansas, 1999.

Arcone, S. A., and N. E. Yankielun, 1.4-GHz radar penetration and evidence of drainage structures in temperate ice: Black Rapids Glacier, Alaska, U. S. A., *J. Glaciol.*, in press, 2001.

Arcone, S. A., N. E. Yankielun, and E. F. Chacho Jr., Reflection profiling of arctic lake ice using microwave FM-CW radar, *IEEE Trans. Geosci. Remote Sens.*, *35*(2), 436–443, 1997.

Bales, R. C., J. R. McConnell, E. Mosley-Thompson, and B. Csatho, Accumulation over the Greenland ice sheet from historical and recent records, *J. Geophys. Res.*, this issue.

Boyne, H. S., and D. A. Ellerbruch, Microwave measurements of snow stratigraphy and water equivalence, paper presented at the 47th Annual Meeting of the Western Snow Conference, Sparks, Nevada, April 18–20, 1979.

Clausen, H. B., C. U. Hammer, J. Christensen, C. Schøtt Hvidberg, D. Dahl-Jensen, M. Legrand, and J. P. Steffensen, 1250 years of global volcanism as revealed by central Greenland ice cores, in *Ice Core Studies of Global Biogeochemical Cycles, NATO ASI Ser.*, vol. I 30, edited by R. J. Delmas, Springer-Verlag, New York, 1995.

Dahl-Jensen, D., N. S. Gundestrup, K. Keller, S. J. Johnsen, S. P. Gogineni, C. T. Allen, T. S. Chuah, H. Miller, S. Kipfstuhl, and E. D. Waddington, A search in north Greenland for a new ice-core drill site, *J. Glaciol.*, *43*(144), 300–306, 1997.

Davis, C. H., C. A. Kluever, B. J. Haines, C. Perez, and Y. Yoon, Improved elevation change measurement of the southern Greenland ice sheet from satellite radar altimetry, *IEEE Trans. Geosci. Remote Sens.*, *38*(3), 1367–1378, 2000.

Fujita, S., and S. Mae, Causes and nature of ice-sheet radio-echo internal reflections estimated from the dielectric properties of ice, *Ann. Glaciol.*, *20*, 80–86, 1994.

Fujita, S., and H. Maeno, S. Uratsuka, T. Furukawa, S. Mae, Y. Fujii, and O. Watanabe, Nature of radio echo layering in the Antarctic ice sheet detected by a two-frequency experiment, *J. Geophys. Res.*, *104*, 13,013–13,024, 1999.

Fujita, S., T. Matsuoka, T. Ishida, K. Matsuoka, and S. Mae, A summary of the complex dielectric permittivity of ice in the megahertz range and its application for radar sounding of polar ice sheets, in *Physics of Ice Core Records*, edited by T. Hondoh, pp. 185–212, Hokkaido Univ. Press, Sapporo, Japan, 2000.

Hammer, C. U., Acidity of polar ice cores in relation to absolute dating, past volcanism, and radio-echoes, *J. Glaciol.*, *25*/93, 359–372, 1980.

Holmgren, J., M. Sturm, N. E. Yankielun and K. Gary, Extensive measurements of snow depth using FM-CW radar, *Cold Regions Science and Technology*, *27*/1, 17–30, 1998.

Intergovernmental Panel on Climate Change (IPCC), Second assessment report: Climate change, Geneva, Switzerland, 1995.

Koh, G., N. E. Yankielun, and A. I. Baptista, Snow cover characterization using multiband FMCW radars, *Hydrol. Process.*, *10*(12), 1609–1617, 1996.

Looyenga, H., Dielectric constants of heterogeneous mixtures, *Physica*, *31*, 401–406, 1965.

McConnell, J. R., G. Lamorey, E. Hanna, E. Mosley-Thompson, R. C. Bales, D. Belle-Oudry, and J. D. Kyne, Annual net snow accumulation over southern Greenland from 1975 to 1998, *J. Geophys. Res.*, this issue.

Millar, D. H. M., Radio-mho layering in polar ice sheets and past volcanic activity, *Nature*, *292*, 441–443, 1981.

Ohmura, A., and N. Reeh, New precipitation and accumulation maps for Greenland, *J. Glaciol.*, *37*(125), 140–148, 1991.

Patterson, W. S. B., *The Physics of Glaciers*, Pergamon, New York, 1994.

Richardson, C., E. Aarholt, S. Hamran, P. Holmlund, and E. Isaksson, Spatial distribution of snow in western Dronning Maud Land, East Antarctica, mapped by a ground-based snow radar, *J. Geophys. Res.*, *102*, 20,343–20,353, 1997.

Saunders, W. K., CW and FM radar, in *Radar Handbook*, 2nd ed., edited by M. I. Skolnik, chap. 14, McGraw-Hill, New York, 1990.

Stove, A. G., Linear FMCW radar techniques, *IEE Proc.-F*, *139*(5), 343–350, 1992.

van der Veen, C. J., and J. F. Bolzan, Interannual variability in net accumulation on the Greenland ice sheet: Observations and implications for mass balance measurements, *J. Geophys. Res.*, *104*, 2009–2014, 1999.

Yankielun, N. E., S. A. Arcone, and R. K. Crane, Thickness profiling of freshwater ice using a millimeter-wave FM-CW radar, *IEEE Trans. Geosci. Remote Sens.*, *30*(5), 1094–1100, 1992.

Yee, K. S., Numerical solution of initial boundary value problems involving Maxwell's equations in isotropic media, *IEEE Trans. Antennas Propag.*, *AP-14*(3), 302–307, 1966.

S. P. Gogineni, and P. Kanagaratnam, Radar Systems and Remote Sensing Laboratory, University of Kansas, 2335 Irving Hill Road, Lawrence, KS 66045-7612. (gogineni@rsl.ukans.edu)

N. Gundestrup and L. Larsen, Department of Glaciology, University of Copenhagen, DK-2100, Copenhagen, Denmark.

(Received August 6, 2000; revised March 12, 2001;
accepted March 21, 2001.)